RESEARCH ARTICLE

NANO · MICRO small
www.small-journal.com

Optimizing C—C Coupling on Cu^0/Cu^+/Ga Interfaces by Enhancing Active Hydrogen Absorption for Excellent CO_2-to-C_{2+} Electrosynthesis

Xiaoshuang Qi, Yikai Yang, Yupeng Lan, Xiuming Bu, Siwei Yang, Di Yin, Hongwen Huang,* Johnny C. Ho,* and Xianying Wang**

The electrocatalytic reduction of CO_2 (CO_2RR) to high-value chemicals and fuels offers a promising route for a clean carbon cycle. However, it often suffers from low catalytic activity and poor selectivity. Heterostructure construction has been shown to be an effective strategy for producing multi-carbon products, but the synergistic mechanisms between multiple active sites resulting from the reconstruction process remain unclear. In this study, a Ga_2O_3/CuO heterostructure is established via a simple sol–gel method to produce C_{2+} products. Experimental results demonstrate that Ga_2O_3 stabilizes Cu^+ to form Cu^0/Cu^+/Ga active centers and enhances water-splitting ability during the reaction. The improved hydrogen absorption on the Ga site shifts the C—C coupling reaction pathway from *OCCO to the asymmetric *OCCHO coupling path with a lower energy barrier. As a result, the catalysts exhibit superior CO_2RR performance, achieving a 70.1% C_{2+} Faradaic efficiency at −1.2 V_{RHE} in a flow cell, with ethylene Faradaic efficiency reaching 58.3% and remaining stable for 10 h.

1. Introduction

Using renewable energy sources for the CO_2 reduction reaction (CO_2RR) to produce carbon-based fuels and chemicals is a promising solution to environmental pollution and the energy crisis.[1–3] Compared with C_1 products (such as methanol, formic acid, and carbon monoxide), C_{2+} products (including ethylene, ethanol, acetic acid, and n-propanol) are more desirable due to their high energy density and economic value.[4–8] Copper-based catalysts are considered promising candidates for converting CO_2 to multi-carbon products because of their moderate adsorption/desorption energy for the intermediate.[9–11] However, their activity and selectivity remain unsatisfactory due to the complex multi-electron transfer steps and the competing hydrogen evolution reaction (HER).

To address this issue, various strategies have been employed to enhance the performance of Cu-based catalysts, including morphology design,[12] surface functionalization,[13] heteroatom doping,[14] and heterostructure construction.[15] Among these, heterostructure construction has proven to be an efficient method for regulating electrocatalytic performance, as demonstrated in systems, such as Cu_2O-BN,[16] CuO/CeO_2,[17] Al–Cu/Cu_2O_3,[18] and NiOOH/Cu.[19] In these heterostructure systems, the supporting material can prevent the complete reduction of CuO to metallic Cu^0, even under cathodic operating voltages greater than the thermodynamic equilibrium potential. Previous experimental and theoretical studies have shown that the interface between Cu^+ and Cu^0 enhances the C—C dimerization step due to the electrostatic attraction between oppositely charged carbon atoms,

X. Qi, H. Huang
College of Materials Science and Engineering
Hunan University
Changsha, Hunan 410082, P. R. China
E-mail: huanghw@hnu.edu.cn

X. Qi, Y. Yang, X. Bu, X. Wang
CAS Key Laboratory of Materials for Energy Conversion
Shanghai Institute of Ceramics
Chinese Academy of Sciences
Shanghai 200050, P. R. China
E-mail: buxiuming@mail.sic.ac.cn; wangxianying@mail.sic.ac.cn

Y. Lan, S. Yang
State Key Laboratory of Materials for Integrated Circuits
Shanghai Institute of Microsystem and Information Technology
Chinese Academy of Sciences
Shanghai 200050, P. R. China

D. Yin, J. C. Ho
Department of Materials Science and Engineering
City University of Hong Kong
Hong Kong SAR 999077, P. R. China
E-mail: johnnyho@cityu.edu.hk

The ORCID identification number(s) for the author(s) of this article can be found under https://doi.org/10.1002/smll.202500538

DOI: 10.1002/smll.202500538

compared to single-component active sites that struggle with the kinetically sluggish C—C coupling process.[20]

However, the supporting materials typically only stabilize the Cu^+ valence state without contributing to the CO_2RR to C_{2+} product formation. Ga-based nanomaterials are excellent electrocatalysts for producing C_1 products and incorporating Ga into Cu-based catalysts has shown excellent overall CO_2RR activity, as seen in Ga single atom-doped CuO,[21] CuGa-II,[22] and Cu_9Ga_4 intermetallic alloys.[23] Thus, constructing Ga_2O_3/CuO heterojunctions may yield highly efficient CO_2RR electrocatalysts for C_{2+} product preparation. To the best of our knowledge, Ga_2O_3/CuO heterostructures have not been reported, and the synergistic mechanisms between multiple active sites resulting from the reconstruction process remain unclear.

In this work, we synthesize a Ga_2O_3/CuO heterostructure electrocatalyst via the sol–gel method to produce C_{2+} products. Characterization results confirm that Ga_2O_3 stabilizes Cu^+ species even at −1.2 V_{RHE}. In situ experiments reveal that the absorbed $^*H$ active species on the Ga_2O_3 surface serve as the main sources for $^*CHO$ formation, shifting the C—C coupling reaction pathway from $^*OCCO$ to the asymmetric $^*OCCHO$ with a low energy barrier. Consequently, the catalysts with multiple active sites significantly enhances the C—C coupling kinetics, exhibiting excellent CO_2RR performance for C_{2+} products with a 70.1% Faradaic efficiency at $-1.2V_{RHE}$ in a flow cell. Notably, ethylene Faradaic efficiency reached 58.3% and remains stableover 10 h. Our work enhances understanding the CO_2RR mechanism involving multiple active sites and provides valuable design inspiration for other Cu-based heterostructures.

2. Results and Discussion

The synthesis process of Ga_2O_3/CuO is shown in **Figure 1a**, in which the blue metal hydroxides were synthesized by a co-precipitation method with the $Cu(NO_3)_2{\cdot}3H_2O$ and $Ga(NO_3)_3{\cdot}xH_2O$ serving as the precursors, and then aged at 60 °C to form the final product (detailed preparation process could be found in Experimental Section). X-ray diffraction (XRD) was first employed to investigate the phase and crystal structure information. The results exhibited that the Ga_2O_3/CuO and CuO had similar diffraction peaks, which matched well with CuO reference (PDF#97-008-7125), indicating that the introduced Ga element was not present in a single metal oxide phase (Figure 1b). In addition, the (111) diffraction peak of Ga_2O_3/CuO underwent a slight redshift compared to CuO, indicating the reduction of lattice spacing. Then, the morphology of the samples was visualized using scanning electron microscope images (SEM) and transmission electron microscope images (TEM). For the CuO, a typical spherical nanoparticle with a diameter of ≈160 nm was observed (Figure S1, Supporting Information). After introducing Ga, the product showed nano-aggregates composed of lamellar particles (Figure 1c,d). Furthermore, no lattice fringes of Ga_2O_3 were observed in the high-resolution transmission electron microscopy (HRTEM) image, while dense crystalline/amorphous interfaces were present, and the (111) planes of CuO were found with a lattice spacing of 0.23 nm (Figure 1e). Moreover, with the energy dispersive spectroscopy (EDS) elemental mapping, it was observed that Cu, Ga, and O elements were uniformly distributed throughout the prepared catalyst (Figure 1f–h). The atomic composition of the Ga_2O_3/CuO catalyst was investigated using inductively coupled plasma optical emission spectroscopy (ICP-OES) and X-ray photoelectron spectroscopy (XPS) analysis, which provided bulk composition and surface composition information, respectively. Experimental results demonstrated that the surface phase exhibited a lower Cu:Ga atomic ratio, indicating the enrichment of Ga_2O_3 on the surface (Table S1, Supporting Information).

Since the introduction of Ga significantly affected the morphology, the XPS technique was further performed to assess the surface chemical states and chemical composition. As shown in **Figure 2a**, the high-resolution Cu 2p spectra exhibited two pairs of characteristic peaks: the peaks located at 934.7 and 954.7 eV belonged to the oxidized divalent Cu^{2+}, and the other two peaks (932.9 and 952.7 eV) were ascribed to metallic Cu^0.[24] In addition, strong satellite peaks further suggested that Cu was mainly present in the oxidized state Cu^{2+}. After the introduction of Ga, the intensity ratio between Cu^{2+}/Cu^0 peaks of Ga_2O_3/CuO decreased obviously, which might be the electron transfer from Ga to Cu. In addition, the Auger electron spectroscopy (AES) of the Cu LMM showed that the peak center of Ga_2O_3/CuO (917.4 eV) was negatively shifted by 0.4 eV compared to the peak of CuO (917 eV), further suggesting the local electronic environment change in Ga_2O_3/CuO. Importantly, no Cu^+ peak was observed on both samples, which is consistent with the Cu 2p spectra results (Figure S2, Supporting Information). Then, for the Ga 2p of Ga_2O_3/CuO, two characteristic peaks located at 1144.8 and 1117.8 eV were fitted well with the Ga^{3+}, indicating the existence of the Ga—O bond on the surface. Correspondingly, the O 1s spectrum of Ga_2O_3/CuO (Figure 2c) can be decomposed into three peaks at 532.2, 531.1, and 529.8 eV, which are attributed to the surface adsorbed water (H_2O), hydroxyl (—OH), and lattice oxygen (Ga—O and Cu—O), respectively.[25] Due to the interfacial interaction between Ga—O and Cu—O, the lattice oxygen peak of Ga_2O_3/CuO shifted to a higher energy by 0.3 eV. Afterward, the local coordination environment and electronic structure of Cu and Ga in Ga_2O_3/CuO were analyzed by X-ray absorption spectroscopy (XAS). The X-ray absorption near-edge structure (XANES) results exhibited the Cu *K*-edge of Ga_2O_3/CuO was between standard CuO and Cu_2O, further confirming that Cu obtained electrons from Ga via the Cu—O—Ga interfacial bonds, which was in agreement with XPS observation (Figure 2d). Besides, the extended X-ray absorption fine spectra (EXAFS) (Figure 2e) showed that the two major characteristic peaks of Ga_2O_3/CuO centered at 1.5 and 2.4 Å, consistent with those of the CuO reference sample. After fitting, the coordination number of the Cu—O path was 3.4, indicating the existence of oxygen vacancies (Table S2, Supporting Information). Subsequently, the wavelet transforms of Cu *K*-edge EXAFS analysis confirm that the main signal at 4.4 $Å^{-1}$ belongs to Cu—O, while the main signal at 6.6 $Å^{-1}$ belongs to Cu—Cu (Figure 2f; Figure S3, Supporting Information). In addition, the Ga *K*-edge XANES showed that the Ga in Ga_2O_3/CuO had a similar crystal structure with Ga_2O_3 reference (Figure 2g). Furthermore, the EXAFS spectrum of Ga *K*-edge in Ga_2O_3/CuO presented the distinct Ga—O coordination peak only at 1.5 $Å^{-1}$. In contrast, a weak Ga—Ga coordination signal was detected, proving Ga existed as a Ga_2O_3 phase in the material (Figure 2h). Based on the fitting results, the coordination number of Ga—O was 4.8, suggesting

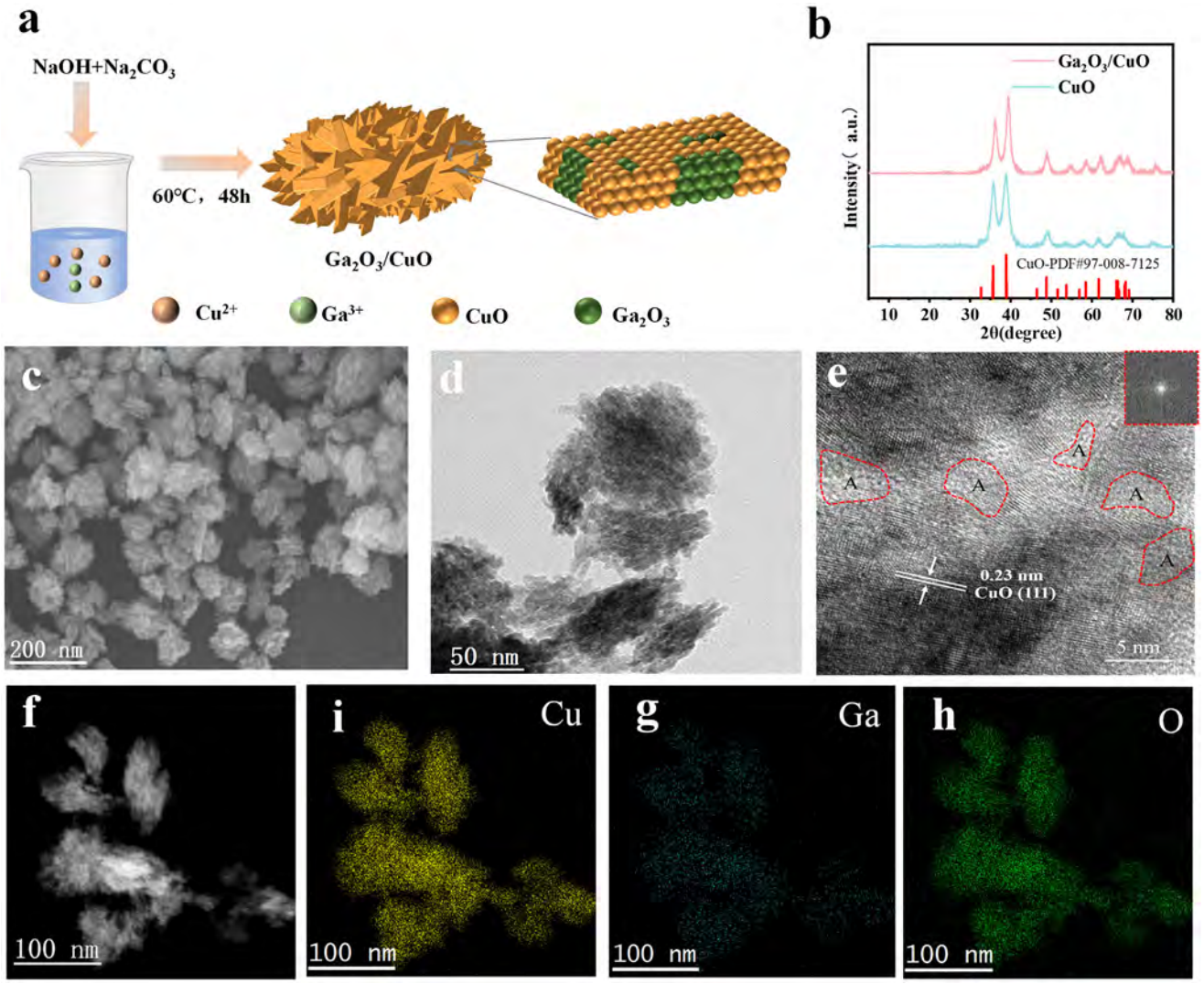

Figure 1. Synthesis and characterization of Ga_2O_3/CuO. a) Schematic illustration of Ga_2O_3/CuO. b) XRD pattern of Ga_2O_3/CuO and CuO. c) SEM and d) TEM images of Ga_2O_3/CuO. e) HRTEM image of Ga_2O_3/CuO. f) STEM image and i–h) corresponding EDS elemental mapping of Ga_2O_3/CuO catalyst.

the presence of a large number of oxygen vacancies, which was consistent with amorphous characteristics (Table S3, Supporting Information). Subsequently, the wavelet transforms of Ga *K*-edge EXAFS also confirm the above conclusion. The wavelet transformation value of the sample is up to 5 $Å^{-1}$, consistent with the Ga—O coordination signal (Figure 2i; Figure S4, Supporting Information).

To shed light on the prepared Ga_2O_3/CuO, the CO_2RR electrochemical properties were evaluated with a flow cell configuration in a 1 M KOH electrolyte. The measured linear scanning voltammetric curve (LSV) in the Ar and CO_2 atmosphere is shown in **Figure 3a**. The LSV results showed that Ga_2O_3/CuO had a lower onset potential under the Ar atmosphere, indicating that Ga_2O_3 resulted in an enhanced kinetic activity for HER. When CO_2 gas was passed, Ga_2O_3/CuO had a greater total current density and lower onset potentials than CuO, indicating a better electron transport ability and CO_2 reduction performance. Then, the catalytic selectivity was evaluated in the applied potential range of −0.8 to −1.6 V_{RHE}. Gas and liquid products were quantitatively tested by gas chromatography (GC) and nuclear magnetic resonance spectrometer (NMR), respectively. The gas products are CO, H_2, and C_2H_4, and the liquid products mainly include HCOOH and CH_3CH_2OH (EtOH) (Figures S5 and S6, Supporting Information). Compared with CuO, Ga_2O_3/CuO showed better selectivity for C_2H_4 in the range of −0.8 to −1.6 V_{RHE}, which has the largest FE_{C2+} of 70.1% and FE_{C2H4} of 58.3% at −1.2 V_{RHE}, while the FE_{C2+} and FE_{C2H4} of CuO is only 52.4% and 42.5% (Figure 3b,c). Moreover, the Ga_2O_3/CuO composite demonstrated significantly reduced hydrogen evolution reaction (HER) activity at more negative potentials, as evidenced by electrochemical characterization data (Figure S7, Supporting Information). Meanwhile, Ga_2O_3/CuO catalysts with different Ga concentrations were also synthesized for the CO_2RR performance. Among them, the best C_2H_4 selectivity was obtained when the

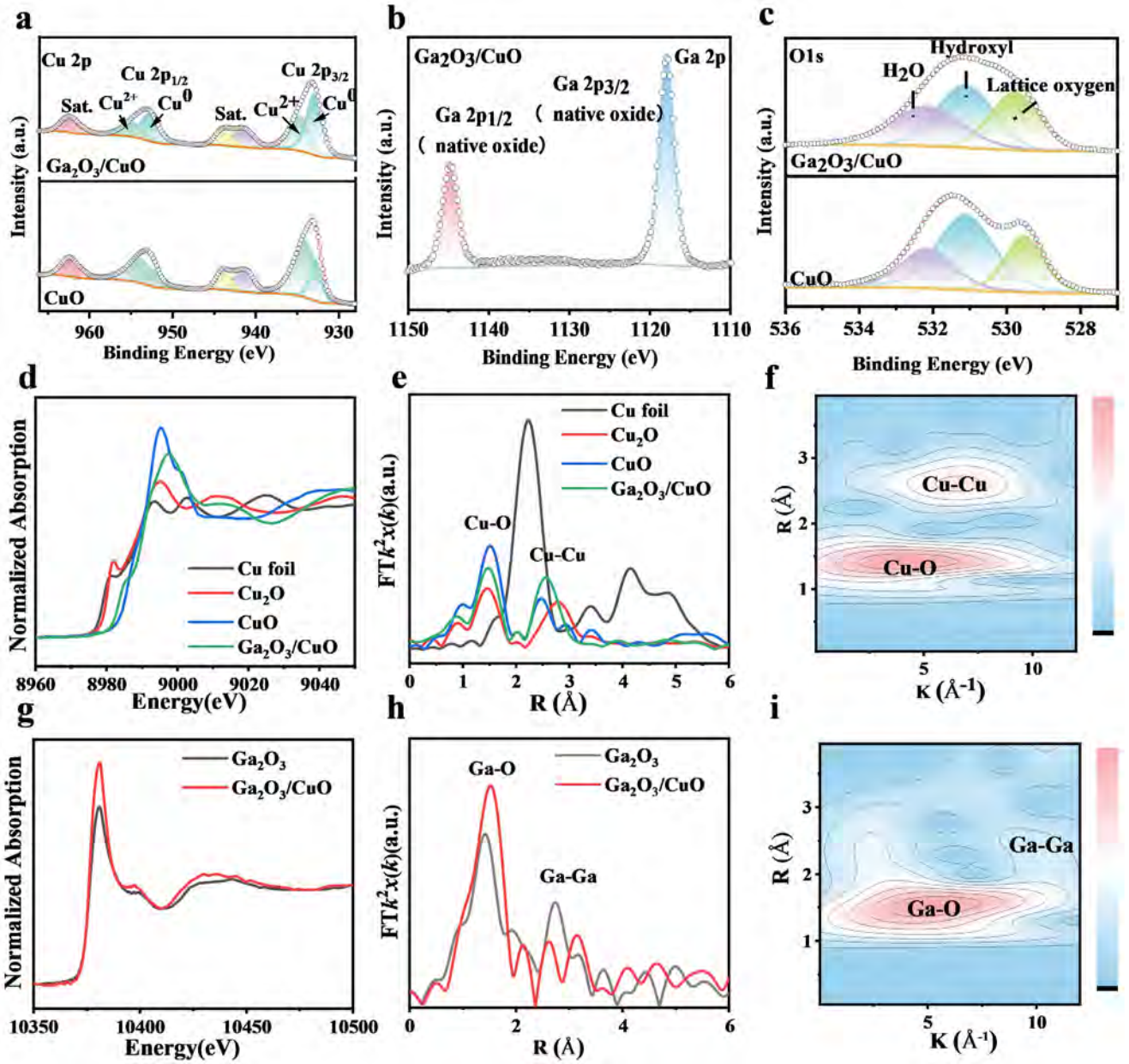

Figure 2. a) Cu 2p, b) Ga 2p, and c) O 1s XPS spectra of Ga_2O_3/CuO and CuO. d) Cu *K*-edge XANES spectra of Ga_2O_3/CuO and CuO. e) Cu *K*-edge Fourier-transformed EXAFS spectra of Ga_2O_3/CuO and CuO. g) Ga *K*-edge XANES spectra of Ga_2O_3/CuO and Ga_2O_3. h) Ga *K*-edge Fourier-transformed EXAFS spectrum of Ga_2O_3/CuO and Ga_2O_3. f) Cu *K*-edge and i) Ga *K*-edge Wavelet transformation of EXAFS plot of Ga_2O_3/CuO.

feedstock ratio of Cu/Ga was 9/4 (Figure S8, Supporting Information). Then, to compare the electrocatalytic performance on the C_2H_4 conversion, the partial current densities of C_2H_4 at different potentials were calculated for Ga_2O_3/CuO and CuO, respectively. At −0.8 V_{RHE}, Ga_2O_3/CuO had similar C_2H_4 current densities (≈70 mA cm^{-2}) to CuO.As the potential increased, the partial current density of C_2H_4 enhanced at a much faster rate, reaching 473.5 mA cm^{-2} at −1.6 V_{RHE} (Figure 3d). The electrochemically active specific surface area (ECSA) of the materials was also obtained in the non-Faraday region: the double-layer capacitance) C_{dl} of Ga_2O_3/CuO was 0.220 mF cm^{-2}, which was larger than that of CuO (0.154 mF cm^{-2}) (Figure S9, Supporting Information). Afterward, the Ga_2O_3/CuO catalyst was tested for stability at −1.2 V_{RHE}, which maintained excellent stability both on FE_{C2H4} (>50%) and current density (≈300 mA cm^{-2}) for 10 h compared to CuO (Figure 3e; Figure S10, Supporting Information). In addition, Ga_2O_3/CuO also showed excellent catalytic performance compared to the reported catalysts for converting CO_2 to C_2H_4 (Figure 3f; Table S4, Supporting Information).[26–33]

To further elucidate the capability of Ga_2O_3/CuO for stable and efficient C_2H_4 production capacity, comprehensive post-reaction physical characterization of the stability-tested samples is

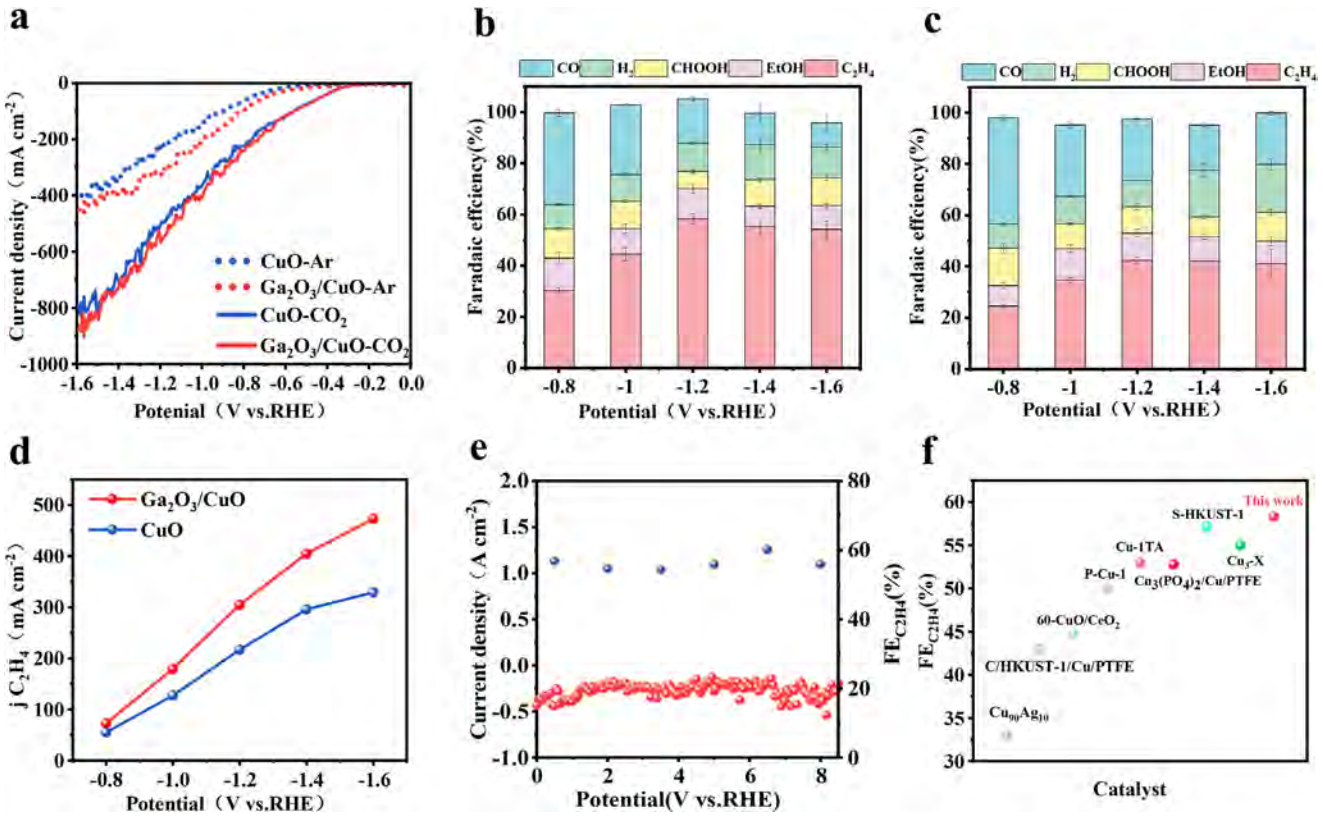

Figure 3. a) LSV curves in CO_2- and Ar- saturated 1 M KOH solutions using a flow cell configuration. b) Product selectivity of Ga_2O_3/CuO. c) Product selectivity of CuO. d) The partial current density of C_2H_4 in the range of −0.8 to −1.6 V_{RHE}. e) Ga_2O_3/CuO was tested by chrono-amperometry with a potential of −1.2 V_{RHE}. f) C_2H_4 Faradaic efficiency compared with recent reports.

essential. Consequently, the samples subjected to a 10 h stability assessment at −1.2 V_{RHE} were systematically analyzed via SEM, XRD, and XPS. First, the SEM images showed Ga_2O_3/CuO was turned into a spherical nanoparticle, similar to CuO (**Figure** 4a; Figure S11, Supporting Information). A similar morphology could rule out performance enhancement resulting from morphological differences.[34] Then, the post-CO_2RR XRD pattern exhibited Ga_2O_3/CuO sample was the Cu/Cu_2O composite while only the metallic Cu^0 phase presented in the original CuO sample, indicating the introduction of Ga_2O_3 could stabilize the Cu^+ phase even when the working potential was −1.2 V_{RHE} (Figure 4b).[17] By comparing the XPS spectra of the initial sample and after CO_2RR, a redshift in the Cu/Cu^+ peak and a weak satellite peak were observed in the XPS spectrum of Ga_2O_3/CuO sample (Figure 4c), indicating the existence of Cu^+ species on the surface.[14] The completely disappeared satellite peak for the CuO sample suggested the surface was composed of metallic Cu. Meanwhile, the Ga 3d XPS spectrum of Ga_2O_3/CuO is negatively shifted by 2.5 eV, indicating the phase transformation from Ga_2O_3 to metallic Ga (Figure S12, Supporting Information). In addition, a series of in situ electrochemical experiments was conducted to monitor the dynamics of the reaction process. Since a better HER and CO_2RR performance was achieved for the Ga_2O_3/CuO sample in the Ar and CO_2 atmosphere (Figure 3a), the surface pH variation was monitored via in situ Raman spectroscopy to investigate the effect of $^*H$ intermediates during the CO_2RR process. As shown in Figure 4d,e, Ga_2O_3/CuO and CuO were tested in the range of 0 ~ −1.0 V_{RHE} in 1 M KOH, the Raman peak areas of dissolved HCO_3^- (1015 cm^{-1}) and CO_3^{2-} (1065 cm^{-1}) were related to their concentrations in solution. The HCO_3^- and CO_3^{2-} concentrations can be used to approximate the electrode surface pH, which agrees with the Henderson–Hasselbalch equations (Figure S13, Supporting Information). For these two samples, the CO_3^{2-} peak decreased, and the HCO_3^- peak gradually strengthened when the potential decreased from 0 to −1.0 V_{RHE}, proving a decrease in the surface pH value. Specifically, Ga_2O_3/CuO and CuO maintain a similar pH value at the potential decrease from 0 to −0.4 V (Figure 4c). While the potential shifted further negatively, the pH on the CuO surface decreased to 9.4 at −1.0 V_{RHE}. In contrast, the surface pH of the Ga_2O_3/CuO decreased from 10.1 to 9.2. As discussed above, the Ga_2O_3/CuO exhibited a better HER performance in the Ar atmosphere, indicating that Ga_2O_3 could enhance water dissociation and surface OH^- concentration.[21] When CO_2 was introduced, abundance OH^- and CO_2 reacted to generate HCO_3^- (Ga_2O_3/CuOshowed a higher HCO_3^-/CO_3^{2-} peak area ratio in Raman spectra), then HCO_3^- reacted with OH^- to generate CO_3^{2-}. Because the surface of the Ga_2O_3 modified CuO has three active sites for CO_2 adsorption: metallic Cu^0, Cu^+ and Ga, and previous theory and experiments suggested that the Cu^+/Cu interface is more favorable for the CO_2 molecular dynamics and thermodynamic adsorption, which leads to the

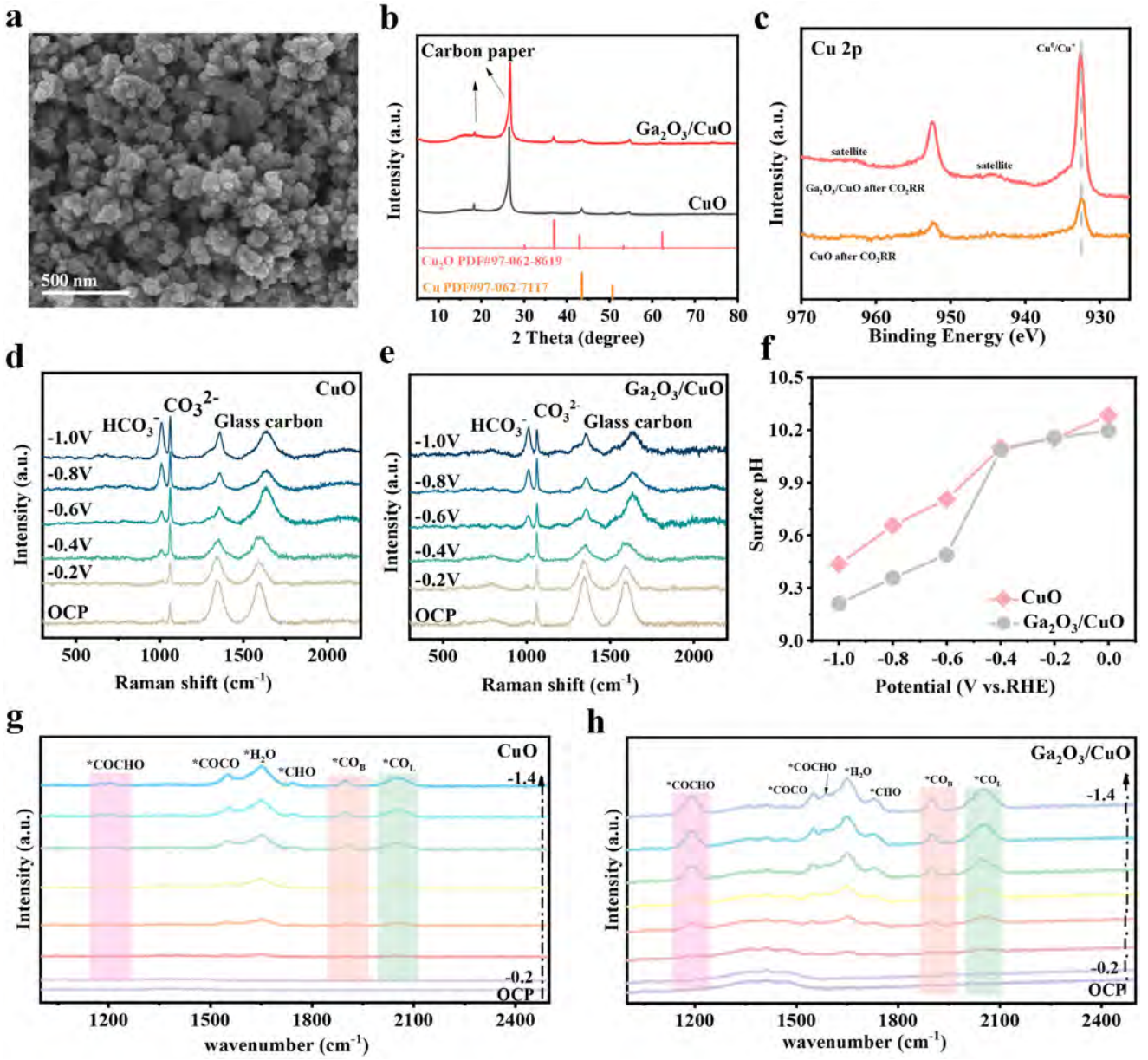

Figure 4. a) SEM image of Ga_2O_3/CuO after CO_2RR. b) XRD pattern after CO_2RR. c) Cu 2p XPS spectra of Ga_2O_3/CuO and CuO. In situ Raman spectra obtained from d) CuO and e) Ga_2O_3/CuO electrodes biased from open circuit voltage (OCV) to −1.0 V_{RHE}. f) pH values calculated from the in situ Raman spectra at various applied potentials ranging from 0 to −1.0 V_{RHE}. In situ ATR-SEIRAS spectra of g) CuO and h) Ga_2O_3/CuO electrodes at various applied potentials ranging from OCV to −1.4 V versus RHE.

adsorption of CO_3^- in the form of C intermediates on the Cu^+ surface, and thus results in the reduction of the concentration of CO_3^{2-} as well as the pH value on the surface.[20]

In addition, to explore the catalyst surface intermediate species and their variations in the CO_2RR reaction process, in situ attenuated total reflection-surface-enhanced IR absorption spectroscopy (ATR-SEIRAS) was performed. As shown in Figure 4g,h, the bridge-bond $^*CO$ (CO_B) and atop-adsorbed $^*CO$ (CO_L) peaks were observed at 1906 and 2056 cm^{-1}, respectively.[35] Moreover, the $^*C$—O (CO_B and CO_L) intermediate concentration on the catalyst surface gradually increased with the increasing working potential. For the Ga_2O_3/CuO sample, a more pronounced enhancement trend was observed compared to CuO, confirming the existence of Ga_2O_3 was beneficial for improving surface $^*CO$ coverage, facilitating the subsequent coupling porcess. Meanwhile, a sharper $^*CHO$ intermediate peak was observed at 1731 cm^{-1} for Ga_2O_3/CuO species, which was the key intermediate for the realization of $^*CO$—CHO asymmetric coupling.[36] $^*CHO$ is formed by the transformation of $^*CO$ after protonation; normally, there are two sources of protons, adsorbed $^*H$ intermediates on the Ga surface and HCO_3^- in solution. Since it was observed that in Ga_2O_3/CuO samples, the

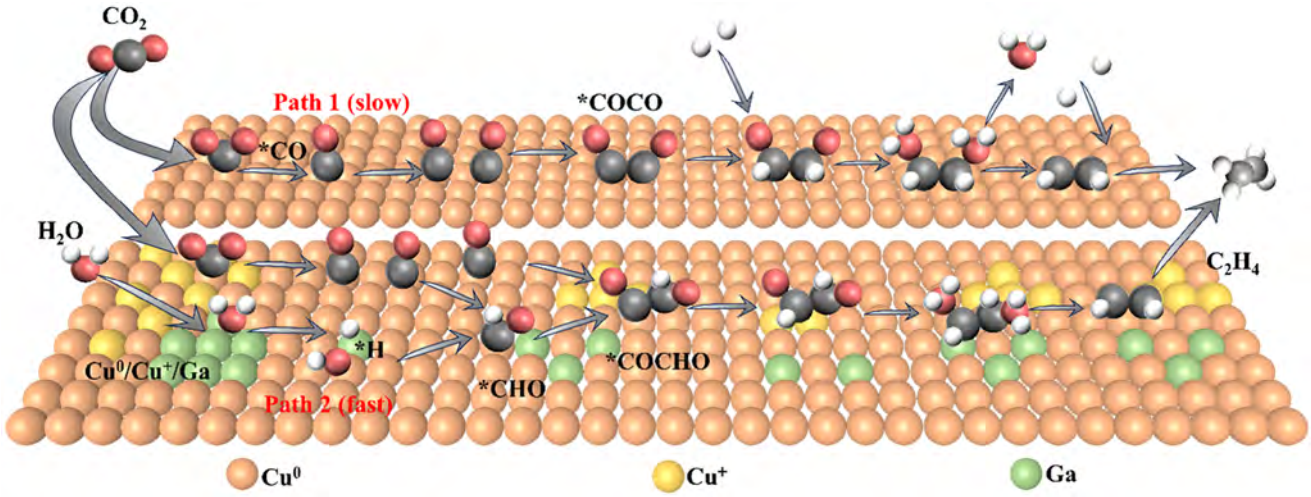

Figure 5. The model reaction route of Ga_2O_3/CuO and CuO.

HER reaction was suppressed with increasing voltage and the pH of the catalyst surface decreased, the source of protonation was mainly the stabilized *H intermediates adsorbed on the Ga surface. The protonation of *CO to form *CHO intermediates consumes the *H species via the hydrogen spillover from the Ga site to the Cu/Cu^+ site, thereby suppressing the enhancement of Faradaic Efficiency of H_2 at the larger cathodic potential. This phenomenon aligns with the dynamic competition between CO_2RR intermediates stabilization and parasitic hydrogen evolution in oxide-modified copper-based systems under cathodic polarization. Corresponding, the *COCO and *CO—*CHO adsorption peaks were observed at 1562, 1584, and 1191 cm^{-1} enhanced significantly. Importantly, the distinct *COCHO peak was only observed on the Ga_2O_3/CuO catalyst, indicating the C_2H_4 reaction path was different from the original CuO sample.[35,37]

Based on the above characterization results, the reaction pathways of C_2H_4 over Ga_2O_3/CuO and CuO are as follows (**Figure 5**). For CuO, under reducing potentials, it undergoes a complete phase transition to metallic Cu^0. The C_2H_4 formation proceeds via *CO—*CO symmetric coupling, with protons for the final product sourced from Cu's inherent HER. As shown in Figure 3a, the HER activity of CuO is notably lower than that of Ga_2O_3/CuO. Consequently, the high energy barrier of *CO—*CO symmetric coupling, combined with the sluggish HER kinetics of Cu itself, limits the production efficiency of C_2H_4. In contrast, for Ga_2O_3/CuO, the introduction of Ga_2O_3 suppresses the complete phase transition of CuO to metallic Cu^0, resulting in a coexisting Cu/Cu^+ state. Simultaneously, Ga^{3+} is reduced to metallic Ga under the same conditions, forming a Cu^+/Cu^0/Ga multiphase interface. The presence of the Cu^+/Cu^0 interface significantly enhances the catalyst's ability to activate and adsorb CO_2. Meanwhile, Ga exhibits exceptional water dissociation capability, leading to the accumulation of abundant *H species on the surface. These *H species act as proton donors, facilitating the critical *CHO intermediate formation. Thus, for Ga_2O_3/CuO, C_2H_4 is primarily generated through the asymmetric coupling of *CO—*CHO. The lower Gibbs free energy associated with asymmetric coupling, coupled with the surface-enriched *H species, synergistically contributes to higher C_2H_4 production efficiency.

3. Conclusion

In this work, Ga_2O_3/CuO heterostructure electrocatalysts were fabricated via a simple sol–gel method to obtain C_{2+} products. The in situ and ex situ characterization results suggest that introducing Ga_2O_3 can accelerate water dissociation and stabilize Cu^+ even at −1.2 V_{RHE} via the strong electronic interaction. Notably, the absorbed *H active species of the Ga site served as the main sources of *CHO formation, thereby forming C_2H_4 from a symmetric coupling path of *CO—CO to an asymmetric coupling path of *CO—CHO. As a result, the obtained catalysts exhibited a superior CO_2RR performance with a 70.1% C_{2+} Faradaic efficiency at −1.2 V_{RHE} in a flow cell, in which the ethylene Faradaic efficiency reached 58.3% and remained stable for 10 h. Our work benefits the understanding of multi-site CO_2RR mechanisms and provides valuable design inspiration for other Cu-based heterostructure construction.

Supporting Information

Supporting Information is available from the Wiley Online Library or from the author.

Acknowledgements

X.Q. and Y.Y. contributed equally to this work. This work was financially supported by the Shanghai Sailing Program (23YF1455000) and the City University of Hong Kong (Project no. 7020088 and 7006109).

Conflict of Interest

The authors declare no conflict of interest.

Data Availability Statement

The data that support the findings of Author: Please check funding information and confirm its correctness. this study are available from the corresponding author upon reasonable request.

Keywords

asymmetric coupling, Cu^+/Cu^0, electrocatalytic CO_2 reduction, ethylene

Received: January 14, 2025
Revised: February 23, 2025
Published online: March 5, 2025

[1] E. W. Lees, B. A. W. Mowbray, F. G. L. Parlane, C. P. Berlinguette, *Nat. Rev. Mater.* **2022**, *7*, 55.
[2] B. Chang, H. Pang, F. Raziq, S. Wang, K.-W. Huang, J. Ye, H. Zhang, *Energy Environ. Sci.* **2023**, *16*, 4714.
[3] G. Wang, J. Chen, Y. Ding, P. Cai, L. Yi, Y. Li, C. Tu, Y. Hou, Z. Wen, L. Dai, *Chem. Soc. Rev.* **2021**, *50*, 4993.
[4] Y. Lei, Z. Wang, A. Bao, X. Tang, X. Huang, H. Yi, S. Zhao, T. Sun, J. Wang, F. Gao, *Chem. Eng. J.* **2023**, *453*, 139663.
[5] T. Zheng, K. Jiang, H. Wang, *Adv. Mater.* **2018**, *30*, 1802066.
[6] T. Lu, T. Xu, S. Zhu, J. Li, J. Wang, H. Jin, X. Wang, J. Lv, Z. Wang, S. Wang, *Adv. Mater.* **2023**, *35*, 2310433.
[7] Q. Chen, X. Wang, Y. Zhou, Y. Tan, H. Li, J. Fu, M. Liu, *Adv. Mater.* **2024**, *36*, 2303902.
[8] J. Gao, Z. Han, X. Wang, L. Wang, Y. Guo, C. Cui, D. Han, L. Zhi, Q.-H. Yang, Z. Weng, *ACS Catal.* **2023**, *13*, 15457.
[9] B. Cao, F.-Z. Li, J. Gu, *ACS Catal.* **2022**, *12*, 9735.
[10] C. Liu, R. Guo, H. Zhu, H. Cui, M. Liu, W. Pan, *J. Mater. Chem. A* **2024**, *12*, 31769.
[11] S. You, J. Xiao, S. Liang, W. Xie, T. Zhang, M. Li, Z. Zhong, Q. Wang, H. He, *Energy Environ. Sci.* **2024**, *17*, 5795.
[12] W. Fang, R. Lu, F.-M. Li, C. He, D. Wu, K. Yue, Y. Mao, W. Guo, B. You, F. Song, T. Yao, Z. Wang, B. Y. Xia, *Angew. Chem. Int. Ed.* **2024**, *63*, 202319936.
[13] M. Fan, J. E. Huang, R. K. Miao, Y. Mao, P. Ou, F. Li, X.-Y. Li, Y. Cao, Z. Zhang, J. Zhang, Y. Yan, A. Ozden, W. Ni, Y. Wang, Y. Zhao, Z. Chen, B. Khatir, C. P. O'Brien, Y. Xu, Y. C. Xiao, G. I. N. Waterhouse, K. Golovin, Z. Wang, E. H. Sargent, D. Sinton, *Nat. Catal.* **2023**, *6*, 763.
[14] X. Liu, T. Liu, T. Ouyang, J. Deng, Z.-Q. Liu, *Angew. Chem. Int. Ed.* **2024**, *64*, 202419796.
[15] J. Yin, Z. Gao, F. Wei, C. Liu, J. Gong, J. Li, W. Li, L. Xiao, G. Wang, J. Lu, L. Zhuang, *ACS Catal.* **2022**, *12*, 1004.
[16] Y. Zhou, Y. Yao, R. Zhao, X. Wang, Z. Fu, D. Wang, H. Wang, L. Zhao, W. Ni, Z. Yang, Y.-M. Yan, *Angew. Chem. Int. Ed.* **2022**, *61*, 202205832.
[17] S. Chu, X. Yan, C. Choi, S. Hong, A. W. Robertson, J. Masa, B. Han, Y. Jung, Z. Sun, *Green Chem.* **2020**, *22*, 6540.
[18] L. Zhang, J. Feng, L. Wu, X. Ma, X. Song, S. Jia, X. Tan, X. Jin, Q. Zhu, X. Kang, J. Ma, Q. Qian, L. Zheng, X. Sun, B. Han, *J. Am. Chem. Soc.* **2023**, *145*, 21945.
[19] X. Mao, C.-W. Chang, Z. Li, Z. Han, J. Gao, M. Lyons, G. Sterbinsky, Y. Guo, B. Zhang, Y. Wang, X. Wang, D. Han, Q.-H. Yang, Z. Feng, Z. Weng, *Adv. Energy Mater.* **2024**, *14*, 2400827.
[20] H. Xiao, W. A. Goddard, T. Cheng, Y. Liu, *Proc. Natl. Acad. Sci.* **2017**, *114*, 6685.
[21] J. Wang, Q. Ji, H. Zang, Y. Zhang, C. Liu, N. Yu, B. Geng, *Adv. Funct. Mater.* **2024**, *34*, 2404274.
[22] P. Li, J. Bi, J. Liu, Y. Wang, X. Kang, X. Sun, J. Zhang, Z. Liu, Q. Zhu, B. Han, *J. Am. Chem. Soc.* **2023**, *145*, 4675.
[23] S. Yan, Z. Chen, Y. Chen, C. Peng, X. Ma, X. Lv, Z. Qiu, Y. Yang, Y. Yang, M. Kuang, X. Xu, G. Zheng, *J. Am. Chem. Soc.* **2023**, *145*, 26374.
[24] H. Shi, L. Luo, C. Li, Y. Li, T. Zhang, Z. Liu, J. Cui, L. Gu, L. Zhang, Y. Hu, H. Li, C. Li, *Adv. Funct. Mater.* **2024**, *34*, 2310913.
[25] C. Li, Z. Guo, Z. Liu, T. Zhang, H. Shi, J. Cui, M. Zhu, L. Zhang, H. Li, H. Li, C. Li, *ACS Catal.* **2023**, *13*, 16114.
[26] K. Xu, J. Li, F. Liu, W. Xu, T. Zhao, F. Cheng, *Mater. Chem. Front.* **2023**, *7*, 1395.
[27] Y. E. Jeon, Y. N. Ko, J. Kim, H. Choi, W. Lee, Y. E. Kim, D. Lee, H. Y. Kim, K. T. Park, *J. Ind. Eng. Chem.* **2022**, *116*, 191.
[28] C. F. Wen, M. Zhou, P. F. Liu, Y. Liu, X. Wu, F. Mao, S. Dai, B. Xu, X. L. Wang, Z. Jiang, P. Hu, S. Yang, H. F. Wang, H. G. Yang, *Angew. Chem. Int. Ed.* **2022**, *61*, 202111700.
[29] Y.-F. Lu, L.-Z. Dong, J. Liu, R.-X. Yang, J.-J. Liu, Y. Zhang, L. Zhang, Y.-R. Wang, S.-L. Li, Y.-Q. Lan, *Angew. Chem. Int. Ed.* **2021**, *60*, 26210.
[30] D. Nam, O. Shekhah, A. Ozden, C. McCallum, F. Li, X. Wang, Y. Lum, T. Lee, J. Li, J. Wicks, A. Johnston, D. Sinton, M. Eddaoudi, E. H. Sargent, *Adv. Mater.* **2022**, *34*, 2207088.
[31] H.-D. Cai, B. Nie, P. Guan, Y.-S. Cheng, X.-D. Xu, F.-H. Wu, G. Yuan, X.-W. Wei, *ACS Appl. Nano Mater.* **2022**, *5*, 7259.
[32] J. Zhang, Z. Liu, H. Guo, H. Lin, H. Wang, X. Liang, H. Hu, Q. Xia, X. Zou, X. Huang, *ACS Appl. Mater. Interfaces* **2022**, *14*, 19388.
[33] X. Y. Zhang, Z. X. Lou, J. Chen, Y. Liu, X. Wu, J. Y. Zhao, H. Y. Yuan, M. Zhu, S. Dai, H. F. Wang, C. Sun, P. F. Liu, H. G. Yang, *Nat. Commun.* **2023**, *14*, 7681.
[34] K. D. Yang, W. R. Ko, J. H. Lee, S. J. Kim, H. Lee, M. H. Lee, K. T. Nam, *Angew. Chem. Int. Ed.* **2017**, *56*, 796.
[35] Y. Yao, T. Shi, W. Chen, J. Wu, Y. Fan, Y. Liu, L. Cao, Z. Chen, *Nat. Commun.* **2024**, *15*, 1257.
[36] S. Zhu, B. Jiang, W.-B. Cai, M. Shao, *J. Am. Chem. Soc.* **2017**, *139*, 15664.
[37] E. Pérez-Gallent, M. C. Figueiredo, F. Calle-Vallejo, M. T. M. Koper, *Angew. Chem. Int. Ed.* **2017**, *56*, 3621.